PHYSICAL REVIEW B **93**, 214506 (2016)

Electron doping evolution of the magnetic excitations in $NaFe_{1-x}Co_xAs$

Scott V. Carr,[1] Chenglin Zhang,[1] Yu Song,[1] Guotai Tan,[2] Yu Li,[1] D. L. Abernathy,[3] M. B. Stone,[3] G. E. Granroth,[4] T. G. Perring,[5] and Pengcheng Dai[1,2,*]

[1]*Department of Physics and Astronomy, Rice University, Houston, Texas 77005, USA*
[2]*Department of Physics, Beijing Normal University, Beijing 100875, China*
[3]*Quantum Condensed Matter Division, Oak Ridge National Laboratory, Oak Ridge, Tennessee 37831, USA*
[4]*Neutron Data Analysis and Visualization Division, Oak Ridge National Laboratory, Oak Ridge National Laboratory, Oak Ridge, Tennessee 37831, USA*
[5]*ISIS Facility, Rutherford Appleton Laboratory, Chilton, Didcot, Oxfordshire OX11 0QX, United Kingdom*

(Received 15 April 2016; revised manuscript received 17 May 2016; published 13 June 2016)

We use time-of-flight (TOF) inelastic-neutron-scattering (INS) spectroscopy to investigate the doping dependence of magnetic excitations across the phase diagram of $NaFe_{1-x}Co_xAs$ with $x = 0, 0.0175, 0.0215, 0.05$, and 0.11. The effect of electron doping by partially substituting Fe by Co is to form resonances that couple with superconductivity, broaden, and suppress low-energy ($E \leqslant 80$ meV) spin excitations compared with spin waves in undoped NaFeAs. However, high-energy ($E > 80$ meV) spin excitations are weakly Co-doping-dependent. Integration of the local spin dynamic susceptibility $\chi''(\omega)$ of $NaFe_{1-x}Co_xAs$ reveals a total fluctuating moment of 3.6 μ_B^2/Fe and a small but systematic reduction with electron doping. The presence of a large spin gap in Co-overdoped nonsuperconducting $NaFe_{0.89}Co_{0.11}As$ suggests that Fermi surface nesting is responsible for low-energy spin excitations. These results parallel the Ni-doping evolution of spin excitations in $BaFe_{2-x}Ni_xAs_2$ in spite of the differences in crystal structures and Fermi surface evolution in these two families of iron pnictides, thus confirming the notion that low-energy spin excitations coupling with itinerant electrons are important for superconductivity, while weakly doping-dependent high-energy spin excitations result from localized moments.

DOI: 10.1103/PhysRevB.93.214506

I. INTRODUCTION

A common thread in high-transition temperature (high-T_c) copper oxides [1–3] and iron pnictides [Fig. 1(a)] [4,5] is their close proximity to a static antiferromagnetic (AF) ordered parent compound [6–9]. Since magnetism may be responsible for many of the anomalous transport properties and the origin of high-T_c superconductivity in these materials [6], previous efforts were focused on understanding the evolution of magnetism as superconductivity is induced by electron- or hole-doping to their AF parent compounds [3,7–9]. In the case of copper oxides, spin excitations in hole-doped superconductors are marked by an hourglass-like dispersion [3] and a neutron spin resonance coupled with superconductivity [2]. For iron-pnictide superconductors [5], much work over the past several years has focused on understanding the hole- and electron-doping evolution of spin excitations in $BaFe_2As_2$ due to the available large single crystals of these materials suitable for inelastic neutron scattering (INS) experiments [10–31]. In the undoped state, $BaFe_2As_2$ forms a collinear AF structure similar to those shown in Fig. 1(b) below $T_N \approx 140$ K, narrowly preceded by a tetragonal-to-orthorhombic structural phase also below $T_s \approx 140$ K ($T_N \leqslant T_s$) [32,33]. Because of the twinned domains, each orthorhombic and perpendicular to each other [Fig. 1(b)], low-energy spin waves in single-crystal $BaFe_2As_2$ are centered around both AF ordering wave vectors $\mathbf{Q_{AF}} = (\pm 1, 0)$ and $(0, \pm 1)$, respectively, in reciprocal space [Fig. 1(d)]. INS measurements using neutron time-of-flight (TOF) chopper spectrometers have shown that spin waves in $BaFe_2As_2$ extend to about ∼300 meV with local dynamic susceptibility, defined as wave-vector-integrated spin dynamic susceptibility over the dashed diamond area in Fig. 1(d) [8], peaking around 200 meV [22]. When Co or Ni is doped into $BaFe_2As_2$, partially replacing Fe and contributing additional electrons to the FeAs layer, superconductivity is induced [34–37] and static order is gradually suppressed. Additionally, the low-energy ($E < 100$ meV) spin excitations become broader than the spin waves in undoped $BaFe_2As_2$ and couple with superconductivity in the form of a neutron spin resonance similar to the superconducting copper oxides [10–21]. However, high-energy ($E > 100$ meV) spin excitations remain weakly electron-doping-dependent and are reminiscent of spin waves in the undoped $BaFe_2As_2$ [24–29]. In concert, these results suggest that low-energy spin excitations in the electron-doped $BaFe_2As_2$ family of materials arise from itinerant electrons and Fermi surface nesting [38–40], while high-energy spin excitations are related to local moments and are insensitive to changes to the Fermi surface [24,28,29,41–44].

Although INS experiments on the $BaFe_2As_2$ family of iron pnictides over the past several years have established the basic characteristics of the electron- and hole-doping evolution of spin excitations and their coupling to superconductivity [10–31], it is equally important to determine if the features found in the $BaFe_2As_2$ family of materials are universal for other iron-pnictide superconductors. For example, while the maximum T_c (∼20 K) for the electron-doped $NaFe_{1-x}Co_xAs$ family of iron pnictides [45–48] is similar to that for Co/Ni-doped $BaFe_2As_2$ [Fig. 1(a)] [5], it is unclear if the electron-doping evolution of spin excitations in $NaFe_{1-x}Co_xAs$ also behaves similarly to that of $BaFe_{2-x}(Co,Ni)_xAs_2$ [10–30]. From INS experiments on spin waves in the undoped NaFeAs [49], we know that the total magnetic bandwidth in NaFeAs is

*pdai@rice.edu

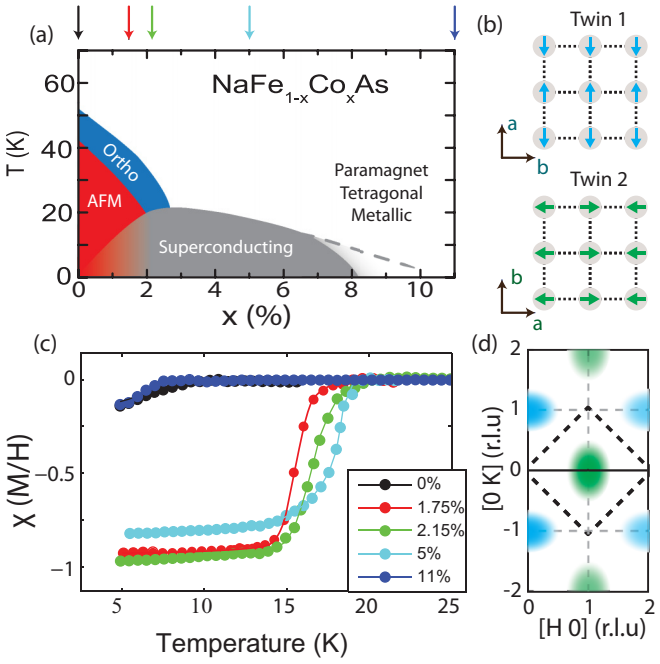

FIG. 1. (a) Schematic phase diagram of NaFeCoAs from thermodynamic measurements [48]. Colored arrows above the figure indicate doping values used in this paper. (b) In-plane magnetic order in twinned orthorhombic domains. (c) dc magnetic susceptibility χ. (d) Neutron scattering schematic indicating intensity at [1,0] and [0,1] originates from different crystal domains.

considerably smaller than that of $BaFe_2As_2$ [50]. This is consistent with the density-functional theory (DFT) combined with dynamical mean-field theory (DMFT) calculation that the increased iron pnictogen height in NaFeAs increases the electron correlations (localizations) and narrows the spin-wave bandwidth compared with $BaFe_2As_2$ [51–53]. If spin excitations are mediating the electron pairing for high-T_c superconductivity, the superconducting condensation energy U should be accounted for by the change in magnetic exchange energy $\Delta E_{\rm ex}(T) = 2J[\langle \mathbf{S}_{i+x} \cdot \mathbf{S}_i \rangle_N - \langle \mathbf{S}_{i+x} \cdot \mathbf{S}_i \rangle_S]$, where J is the nearest-neighbor magnetic exchange coupling and $\langle \mathbf{S}_{i+x} \cdot \mathbf{S}_i \rangle$ is the magnetic scattering in absolute units at the normal (N) and superconducting (S) phases at zero temperature [6], within an isotropic t-J model [54]. Since the effective magnetic exchange coupling constants of NaFeAs [50] are considerably smaller than those of $BaFe_2As_2$ [22], it will be instructive to systematically map out the overall spin excitation spectra in $NaFe_{1-x}Co_xAs$ and compare the result with those of the $BaFe_{2-x}Ni_xAs_2$ family of materials [24,25,28,29]. In previous INS experiments on $NaFe_{1-x}Co_xAs$ probing low-energy spin excitations using triple-axis spectrometry, we find the presence of a single, sharp neutron spin resonance in a sample with nearly optimal Co-doping, similar to the resonance in electron-doped $BaFe_2As_2$ [55], while an underdoped sample with coexisting superconductivity and AF order exhibits a double resonance [56,57]. To illuminate the rest of the story, the Co-doping evolution of high-energy spin excitations in superconducting and nonsuperconducting $NaFe_{1-x}Co_xAs$ needs to be established.

In this article, we report TOF INS studies of the temperature and doping dependence of spin excitations over the entire Brillouin zone (BZ) in $NaFe_{1-x}Co_xAs$. A schematic phase diagram of $NaFe_{1-x}Co_xAs$ is presented in Fig. 1(a), where all high-temperature compounds are paramagnetic metals with a tetragonal structure illustrated by the white region. The white-blue border indicates the tetragonal-to-orthorhombic structural transition, and the red region depicts stripe AF order in the orthorhombic compound. Superconductivity exists in the gray region, where the opaqueness illustrates the superconducting volume fraction. When fully opaque, compounds in the superconducting region are tetragonal and not magnetically ordered. We chose Co-doping concentrations of $x = 0$, 0.0125, 0.0175, 0.0215, 0.05, and 0.11, as shown by the arrows in the electronic phase diagram of $NaFe_{1-x}Co_xAs$ [Fig. 1(a)] [45–48]. Since NaFeAs has a similar orthorhombic AF ground state to that of $BaFe_2As_2$ [Fig. 1(b)] [49], AF Bragg peaks and spin excitations from twinned domains will appear at $\mathbf{Q_{AF}} = (\pm 1, 0)$ and $(0, \pm 1)$ positions in reciprocal space [Fig. 1(d)]. Figure 1(c) shows the temperature dependence of the magnetic susceptibility χ. While the $x = 0$ and 0.11 samples are not bulk superconductors (the slight drop in susceptibility is due to filamentary superconductivity) [47,48], the $x = 0.0175$ ($T_c \approx 16$ K) and 0.0215 ($T_c \approx 18$ K) samples are in the underdoped and nearly optimally doped regime, and $x = 0.05$ is Co-overdoped with $T_c \approx 20$ K [Fig. 1(c)]. T_c is estimated by the onset of steepest descent of χ. This range of Co-doped NaFeAs covers the entire superconducting phase diagram of the system, from undoped NaFeAs to underdoped, near optimally doped, overdoped superconducting, and nonsuperconducting $NaFe_{1-x}Co_xAs$. Compared with spin waves in undoped NaFeAs, we find that Co-doping in NaFeAs slightly elongates the low-energy spin excitations along the transverse direction around the commensurate AF order wave vector. For superconducting samples, a neutron spin resonance forms below T_c consistent with earlier work [55–57]. For Co-overdoped nonsuperconducting $NaFe_{0.89}Co_{0.11}As$, a large spin gap forms in the low-temperature state very similar to Ni-overdoped nonsuperconducting $BaFe_{1.7}Ni_{0.3}As_2$ [28]. By comparing TOF INS data in $NaFe_{1-x}Co_xAs$ with $x = 0$, 0.0125, 0.0175, 0.0215, and 0.05, we establish the Co-doping evolution of the wave vector and energy dependence of the spin excitations throughout the BZ, and we find that high-energy ($E > 80$ meV) spin excitations are weakly Co-doping-dependent. Although the $NaFe_{1-x}Co_xAs$ family of materials has stronger electron correlations and weaker magnetic exchange couplings compared with those of $BaFe_2As_2$-based superconductors, superconductivity-induced changes in spin excitations are still much larger than the superconducting condensation energy. These results are similar to those of $BaFe_2As_2$-based materials, and they are consistent with the idea that magnetic excitations are important for superconductivity of iron-pnictide superconductors.

II. EXPERIMENTAL RESULTS

Our TOF INS experiments were carried out at the wide angular-range chopper spectrometer (ARCS) [58] and fine-resolution Fermi chopper spectrometer (SEQUOIA) [59] at the Spallation Neutron Source (SNS), Oak Ridge National

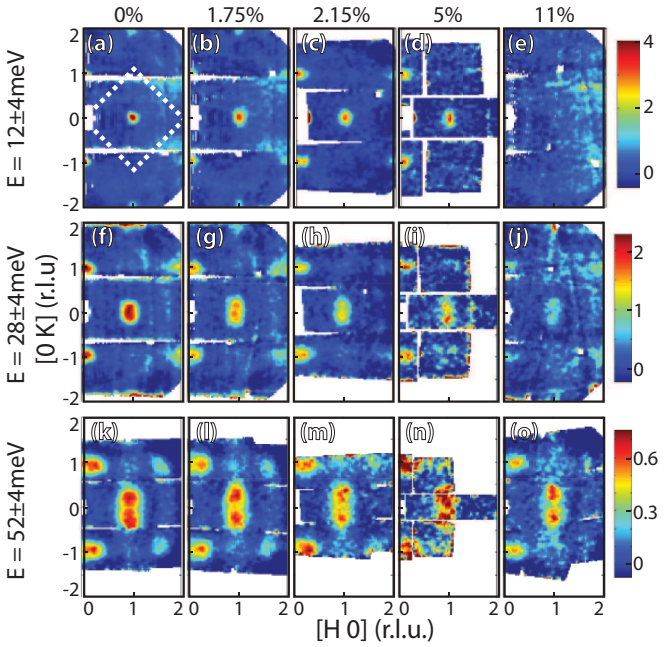

FIG. 2. Two-dimensional slices from ToF INS of $NaFe_{1-x}Co_xAs$ measured with an incident energy of 80 meV at energy transfers of 12 ± 4 meV (a)–(e), 28 ± 4 meV (f)–(j), and 52 ± 4 meV (k)–(o) for doping values $x = 0$, 0.0175, 0.0215, 0.05, and 0.11, respectively. The white box in (a) indicates first magnetic BZ.

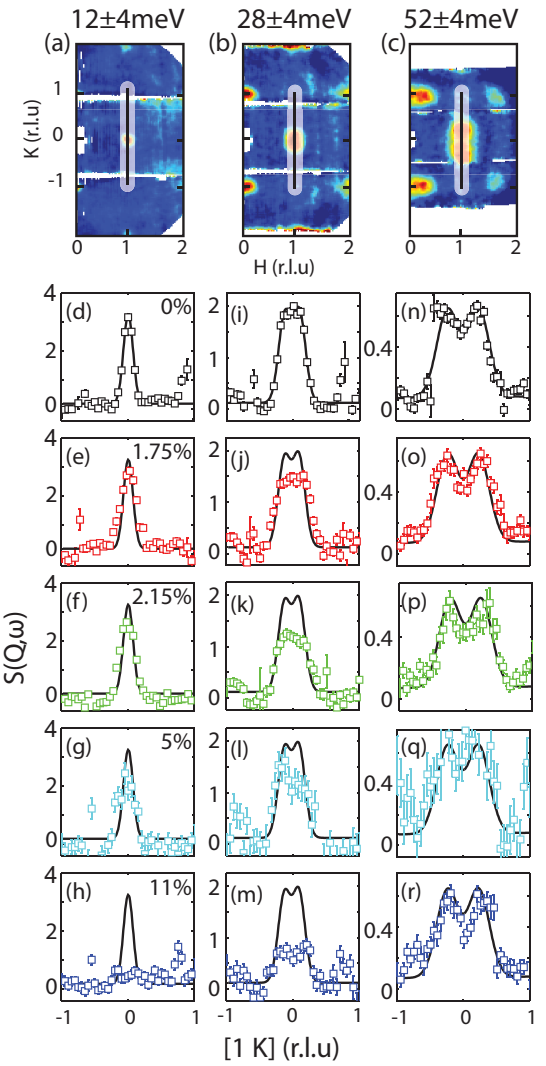

FIG. 3. (a)–(c) Illustrations of one-dimensional transverse cuts from Figs. 2(a), 2(f), and 2(k). Cuts measured with an incident energy of 80 meV at energy transfers of 124 meV (d)–(h), 284 meV (i)–(m), and 524 meV (n)–(r) for doping values $x = 0$, 0.0175, 0.0215, 0.05, and 0.11, respectively. All cuts integrated over $0.9 < H < 1.1$. Black curves are a Gaussian fit to the parent compound at identical energy transfer.

Laboratory (ORNL), and at MAPS chopper spectrometer at the Rutherford-Appleton Laboratory, UK. Large single crystals of $NaFe_{1-x}Co_xAs$ were grown by the self-flux method [55–57]. Since these samples are highly air-sensitive [60], we have protected them with a thin aluminum foil envelope coated with the hydrogen-free amorphous fluoropolymer CYTOP. The mass of the CYTOP was negligible compared to the sample mass, and no scattering features from the glue were observed for the energy range probed ($E > 10$ meV). To compare with spin-wave results in undoped NaFeAs [50] and those of $BaFe_2As_2$ [22], we define the wave vector $\mathbf{Q}$ at (q_x, q_y, q_z) as $(H,K,L) = (q_xa/2\pi, q_yb/2\pi, q_zc/2\pi)$ reciprocal-lattice units (r.l.u.), where $a \approx b \approx 5.56$ Å, and $c = 6.95$ Å. For the $x = 0$, 0.0175, and 0.11 compounds, we used the ARCS spectrometer. The experiments on the $x = 0.0215$ and 0.05 compounds were carried out on the SEQUOIA and MAPS spectrometers, respectively. Crystals were coaligned using CG-1B, a cold neutron alignment station at High-Flux Isotope Reactor (HFIR), and affixed to aluminum plates with aluminum wire. Each sample array was coaligned in the $[H,0,L]$ scattering plane with a mosaic of less than 3 degrees. For each experiment, sample arrays with a total mass of 18, 11, 19, 15, and 10 g for $x = 0$, 0.0175, 0.0215, 0.05, and 0.11, respectively, were loaded into a closed-cycle helium displex with the incident beam parallel to the c axis to display the $[H,K]$ scattering plane. All measurements were performed at the base temperature of 5 K unless otherwise noted. Each sample was measured at different subsets of incident energies in the range $E_i = 25, 35, 50, 80, 150, 250, 350$, and 450 meV, with all compounds measured with $E_i = 80$ and 250 meV. A detailed list of incident energies measured for each doping can be found in Table II located in the Appendix. For direct comparison of spin-wave intensities between samples, each spectrum was first normalized to absolute units (mbarn/sr/meV/f.u.) using a vanadium standard to account for sample mass, then to each other by relative phonon intensity to account for spectrometer differences and residual flux in the sample (see the Appendix). Finally, phonon self-normalization was used to confirm the magnitude of spin-excitation intensities [72].

The neutron-scattering function $S(Q,E)$ is related to the imaginary part of the spin dynamic susceptibility $\chi''(Q,E)$ by correcting for the Bose population factor via $S(Q,E) = 1/\{1 - \exp[-E/(k_BT)]\}\chi''(Q,E)$, where k_B is Boltzmann's constant. We can then calculate the local dynamic susceptibility by using $\chi''(E) = \int \chi''(\mathbf{Q},E)d\mathbf{Q}/\int d\mathbf{Q}$ (in units of μ_B^2/eV/f.u.) with the integration over the BZ noted by

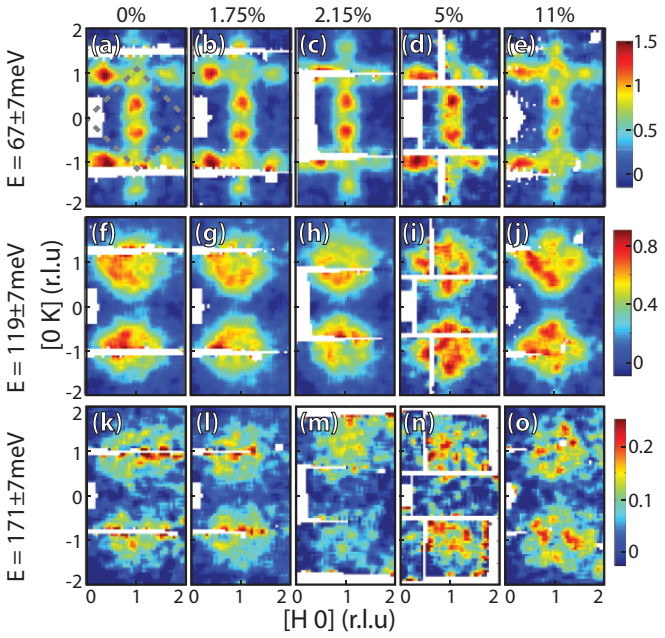

FIG. 4. Two-dimensional slices from ToF INS of $NaFe_{1-x}Co_xAs$ measured with an incident energy of 250 meV at energy transfers of 67 ± 13 meV (a)–(e), 119 ± 13 meV (f)–(j), and 171 ± 13 meV (k)–(o) for doping values $x = 0$, 0.0175, 0.0215, 0.05, and 0.11, respectively.

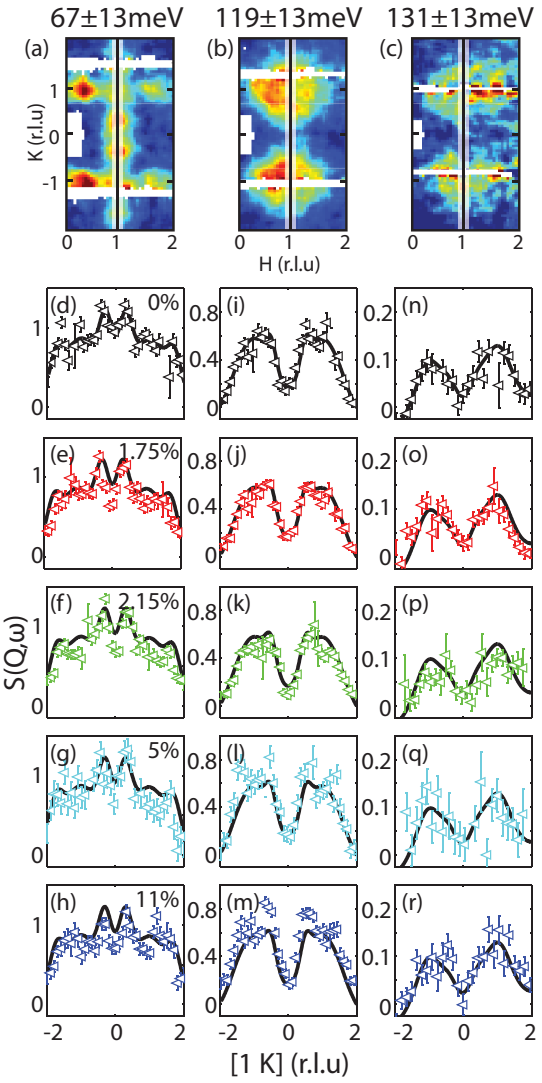

FIG. 5. Illustrations of one-dimensional transverse cuts from Figs. 4(a), 4(f), and 4(k). Cuts measured with an incident energy of 250 meV at energy transfers of 67 ± 13 meV (d)–(f), 119 ± 13 meV (i)–(m), and 171 ± 13 meV (n)–(r) for doping values $x = 0$, 0.0175, 0.0215, 0.05, and 0.11, respectively. All cuts integrated over $0.9 < H < 1.1$. Black line in each row is a Gaussian fitting to the parent compound for peak comparison.

the white outlined region in Fig. 2(a), where $\chi''(\mathbf{Q},E) = (1/3)\mathrm{tr}[\chi''_{\alpha\beta}(\mathbf{Q},E)]$ [17,24]. All calculations require the background to be determined and subtracted before computation. A detailed description of background calculation and subtraction is outlined in the Appendix.

We begin by examining the wave-vector dependence of the two-dimensional (2D) background-subtracted spin-excitation intensities at different energy transfers as a function of increasing Co-doping x. Figure 2 summarizes the data acquired with an incident energy $E_i = 80$ meV at different excitation energies within the $[H,K]$ plane. The horizontal rows show excitation energies of $E = 12 \pm 4$, 28 ± 4, and 52 ± 4 meV, where the $\pm$ values indicate the range of energy integration. The columns show data from $x = 0$, 0.0175, 0.0215, 0.05, and 0.11 in $NaFe_{1-x}Co_xAs$. The white box in Fig. 2(a) illustrates the zone over which the magnetic scattering was integrated to estimate the local dynamic susceptibility $\chi''(E)$. As expected, spin excitations are centered around AF ordering wave vectors $\mathbf{Q_{AF}} = (\pm 1,0)$ and $(0,\pm 1)$. With increasing Co-doping, $E = 12 \pm 4$ meV spin excitations at $\mathbf{Q_{AF}} = (1,0)$ become broader and weaker, and they disappear completely for the $x = 0.11$ nonsuperconducting sample [Figs. 2(a)–2(e)]. Upon increasing the excitation energies to $E = 28 \pm 4$ and 52 ± 4 meV, the situation is similar except that spin excitations now appear for the $x = 0.11$ sample [Figs. 2(f)–2(j) and 2(k)–2(o)]. Figure 3 summarizes one-dimensional cuts of the data along the transverse direction as illustrated in panels (a), (b), and (c). Black curves in Fig. 3 show single Gaussian fits to the excitations in the parent compound NaFeAs ($x = 0$), and are overplotted with cuts from $x = 0.0175$, 0.0215, 0.05, and 0.11 for comparison of scale and peak width. At the lowest probed energy transfer of $E = 12 \pm 4$ meV [Figs. 3(d)–3(h)], it is clear that there is a decrease in peak height and a small increase in peak width, with scattering persisting throughout the superconducting dome and fully gapped in the overdoped $x = 0.11$ compound. This trend persists at $E = 28 \pm 4$ meV [Figs. 3(i)–3(m)] and becomes less apparent at $E = 52 \pm 4$ meV [Figs. 3(n)–3(r)]. At $E = 52 \pm 4$ meV, the differences between different Co-dopings in terms of peak height, width, and splitting are very small. Large discrepancies in magnetic scattering intensity are observed only in small energy transfers with intensities becoming comparable around $E \approx 50$ meV. This observation is reflected in previous measurements in $BaFe_{2-x}Ni_xAs_2$, in which a strong doping dependence is observed below $E \approx 80$ meV [24,25,28,29].

Background-subtracted constant energy transfer images of excitations for $E_i = 250$ meV are shown in Fig. 4, with

columns reflecting the cobalt doping value in the same way as Fig. 2. Constant energy slices at $E = 67 \pm 7$ meV reveal very small changes in intensity and line shape with increasing cobalt doping [Figs. 4(a)–4(e)]. The transverse dispersion from the AF ordering wave vector is clearly visible at all dopings, as is a feature stemming from the zone-boundary wave-vector positions $(\pm 1, \pm 1)$. When energy is increased to $E = 119 \pm 7$ meV, spin excitations form a ringlike structure centered around the wave vector $(\pm 1, \pm 1)$, and again they are weakly Co-doping dependent [Figs. 4(f)–4(j)]. Upon increasing energy to $E = 171 \pm 7$ meV, spin excitations for all Co-doping levels become very weak but are well centered around $(\pm 1, \pm 1)$ [Figs. 4(k)–4(o)].

Figures 5(d)–5(h) show transverse cuts along the $[0, K]$ direction at $E = 67 \pm 13$ meV [Fig. 5(a)], which reveal dispersive spin excitations away from the AF wave vector $\mathbf{Q_{AF}} = (1,0)$ and additional scattering at $(1, \pm 1)$. This additional scattering does not vary with doping, indicating it to be an intrinsic property of the $NaFe_{1-x}Co_xAs$ system. The presence of spin excitations near both wave vectors, $\mathbf{Q_{AF}} = (1,0)$ and $(1,1)$, is a unique feature of $NaFe_{1-x}Co_xAs$ not observed in the $BaFe_{2-x}Ni_xAs_2$ family of materials [22,29]. However, recent TOF INS measurements of the FeSe family of materials reveal spin excitations at both of these wave vectors that are interpreted as a competition between stripe magnetic order and Néel order [61]. The presence of similar features in the $NaFe_{1-x}Co_xAs$ family of materials suggests that magnetic frustrations may also play an important role in determining the rather low Néel temperature and weakly ordered moment of the undoped NaFeAs [49].

At higher-energy transfers the signal becomes increasingly diffuse, shown as broad peaks centered around $(1, \pm 1)$ at $E = 119 \pm 13$ meV [Figs. 5(i)–5(m) and 5(b)] and $E = 171 \pm 13$ meV [Figs. 5(n)–5(r) and 5(c)]. These observations are broadly consistent with results in $BaFe_{2-x}Ni_xAs_2$ [29]. However, whereas spin excitations in the present compounds are already quite diffuse and centered at the zone boundary by 171 meV [Figs. 5(n)–5(r)], indicating the band top of a Heisenberg system, excitations at comparable energies in $BaFe_{2-x}Ni_xAs_2$ remain well defined, indicating a smaller total magnetic excitation bandwidth in the $NaFe_{1-x}Co_xAs$ system. The high-energy spin-excitation intensities, line shapes, and bandwidth are essentially Co-doping independent to the accuracy of our measurements.

To further study the effect of Co-doping on the overall magnetic excitation energy bandwidth, in Fig. 6 we plot Co-doping-dependent projections of the overall spin excitations along the $[H,0]$ and $[1,K]$ directions obtained using $E_i = 250$ meV. Each figure is a compilation of background-subtracted one-dimensional cuts, some of which are featured in Figs. 3 and 5.

We will first examine the transverse spin-excitation dispersions along the $[1,K]$ direction for different Co-doping concentrations. Inspection of the data in Figs. 6(f)–6(j) reveals that the most obvious change with doping is in the low-energy fluctuations. With increased Co-doping, there is a clear, systematic reduction of scattering intensity below 50 meV. Upon reaching the Co-overdoped state when superconductivity is suppressed, no magnetic scattering intensity is visible at small energy transfers due to the presence of a spin gap. For spin excitations above 50 meV, there is no distinct trend with increasing Co-doping, suggesting that the effective magnetic exchange coupling constants are weakly Co-doping-dependent. Figures 6(a)–6(e) plot the Co-doping dependence of the spin excitations projected along the $[H,0]$ direction. Similar to data in Figs. 6(f)–6(j), low-energy spin excitations decrease with increasing Co-doping, and vanish for nonsuperconducting $NaFe_{0.89}Co_{0.11}As$. Additionally, while the excitations are dispersive along the transverse $[1,K]$ direction, there is no dispersive feature longitudinally along the $[H,0]$ direction. This discrepancy highlights the strongly anisotropic nature of the excitations. These features are rather different from traditional spin waves from a local moment Heisenberg Hamiltonian.

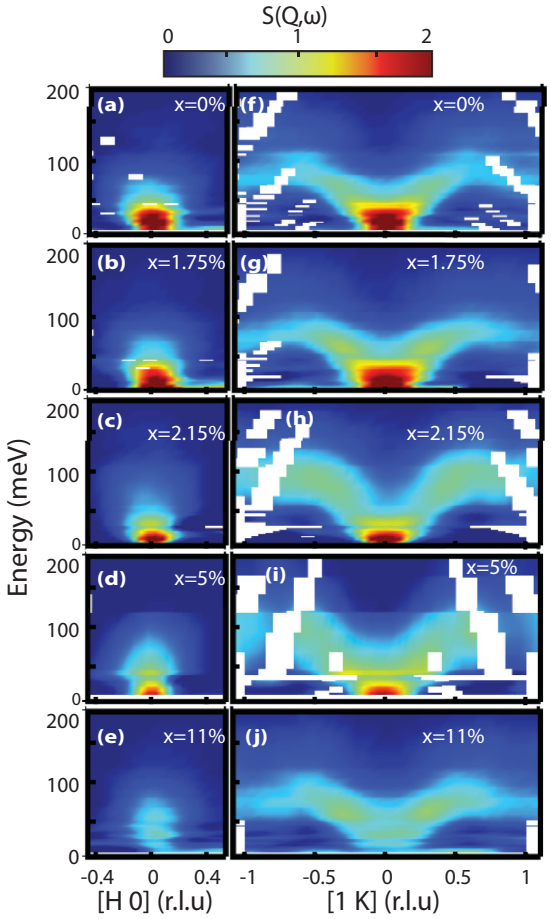

FIG. 6. (a)–(e) Two dimensional Q-E slices of $NaFe_{1-x}Co_xAs$ for $x = 0$, 0.0175, 0.0215, 0.05, and 0.11 along H integrated on the window $K = [-0.10.1]$ r.l.u. in absolute units. (f)–(j) Similar slices along K for $x = 0$, 0.0175, 0.0215, 0.05, and 0.11 integrated across the window $K = [0.91.1]$ r.l.u. All figures use representative data from all incident energies measured and have been smoothed once using nearest-neighbor points.

To further compare the Co-doping evolution of the low-energy spin excitations, we plotted energy dependence of the dynamic susceptibility $\chi''(E)$ obtained by integrating the $E_i \leqslant 250$ meV data over the range $H = 1 \pm 0.1$ and $K = 0 \pm 0.1$ around the AF ordering wave vector $\mathbf{Q_{AF}} = (1,0)$ [Figs. 7(a)–7(e)]. Figures 7(f)–7(j) and 7(k)–7(o)

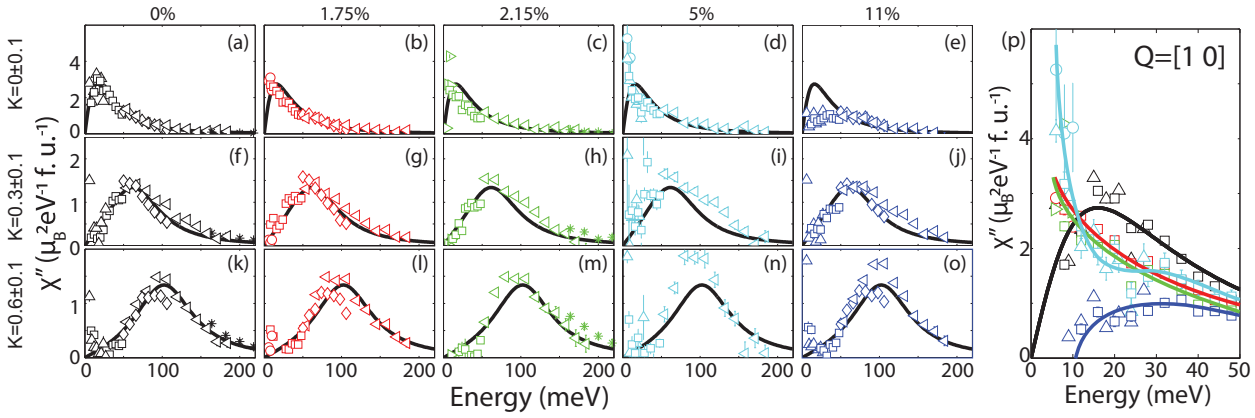

FIG. 7. One-dimensional constant Q cuts obtained by integrating along $H = [0.91.1]$ and (a)–(e) $K = [-0.10.1]$, (f)–(j) $K = [0.20.4]$, and (k)–(o) $K = [0.50.7]$ for dopings of $x = 0$, 0.0175, 0.0215, 0.05, and 0.11, respectively. Black lines are damped harmonic-oscillator fits to parent compound data for comparison. Symbols correspond to incident energy (see Table II). (p) Overplot of low energy constant Q points at the AF wave vector with integration windows of ± 0.1 in both directions. Solid lines are guides to the eye.

show identical cuts **Q**-integrated over $[H = 1 \pm 0.1, K = 0.3 \pm 0.1]$ and $[H = 1 \pm 0.1, K = 0.6 \pm 0.1]$, respectively. The solid lines in the figures are fits to undoped NaFeAs using a damped harmonic-oscillator description of magnetic excitations, $\chi''(E) = A\frac{\Gamma E E_0}{(E^2-E_0^2)^2+4(\Gamma E)^2}$, overplotted on equivalent cuts of other Co-doping concentrations. While the energy dependence of the dynamic susceptibility is weakly Co-doping-dependent in Figs. 7(f)–7(j) and 7(k)–7(o), the low-energy $\chi''(E)$ clearly changes with increasing x in Figs. 7(a)–7(e). Figure 7(p) shows a magnification of the low-energy excitations integrated around $\mathbf{Q_{AF}} = (1,0)$, which clearly reveal a reduction of the low-energy dynamic susceptibility for $NaFe_{0.89}Co_{0.11}As$.

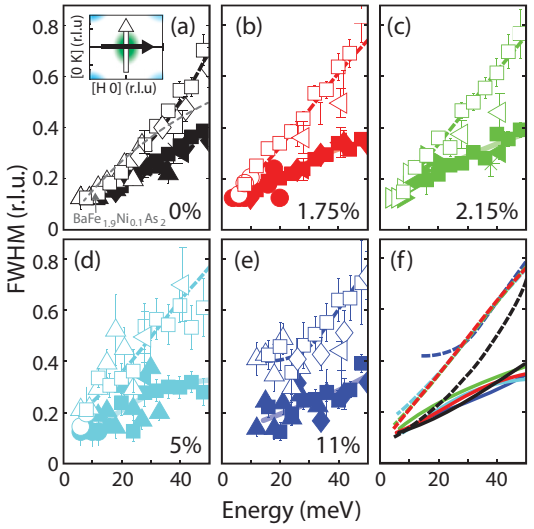

FIG. 8. (a) Inset: schematic showing direction of cuts at the AF wave vector [1 0]. Solid arrow (and points) indicates a longitudinal cut and open arrow (points) indicates a transverse cut. (a)–(e) FWHM of single Gaussian peak fits to constant energy cuts. Dashed and solid lines are guides to the eye for longitudinal and transverse cuts, respectively. (f) Overplot of guides from (b)–(f).

In previous systematic INS studies of the hole-/electron-doping dependence of spin excitations in the $BaFe_2As_2$ family of materials [24–29], it was argued that the wave-vector dependence of low-energy spin excitations arises from nesting between the hole and electron Fermi surfaces. As Co- or Ni-doping to $BaFe_2As_2$ enlarges the electron Fermi surfaces and reduces the hole Fermi surfaces [62], spin excitations become transversely elongated following the doping-induced mismatch between the hole and electron Fermi surfaces [63]. Figure 8 summarizes the full width at half-maximum (FWHM) of spin excitations along the longitudinal [Fig. 8(a) inset and closed symbols in Figs. 8(a)–8(e)] and transverse [Fig. 8(a) inset and open symbols in Figs. 8(a)–8(e)] directions resulting from single Gaussian fits on data below $E = 50$ meV. A direct comparison across dopings can be seen in Fig. 8(f). While solid lines are for the longitudinal FWHM and overlay well, the transverse elongation, shown by dashed lines, increases with increasing Co-doping below $E \approx 40$ meV. For comparison, the transverse FWHM for optimally doped $BaFe_{1.9}Ni_{0.1}As_2$ is plotted in Fig. 8(a) as the dashed line [24]. At low-energy transfers, the FWHM is the same but grows more slowly with energy due to a higher spin-excitation velocity.

To quantitatively compare the Co-doping-dependent dispersion curves of $NaFe_{1-x}Co_xAs$, we plot in Fig. 9 the evolution of spin-excitation dispersions along the $[1,K]$ direction as a function of increasing Co-doping x. Open symbols are peak centers from two Gaussian fits to transverse constant energy cuts through the AF wave vector. Filled symbols are peak centers from constant wave vector cuts such as those shown in Fig. 7. Consistent with data in Fig. 6, we find that Co-doping into NaFeAs broadens the low-energy spin excitations along the transverse direction, but it has little impact on the overall dispersion or spin-excitation bandwidth. This is most clearly illustrated in Fig. 9(f), where dispersions for different Co-dopings are overplotted.

Figures 10(a)–10(e) illustrate the energy and doping dependence of the local dynamic susceptibility $\chi''(E)$ for different Co-doping concentrations. The wave-vector integration range of $\int \chi''(E,\mathbf{Q})dQ / \int dQ$ is shown in the dashed box of Fig. 2(a) [8]. Solid lines in the figures are a combination

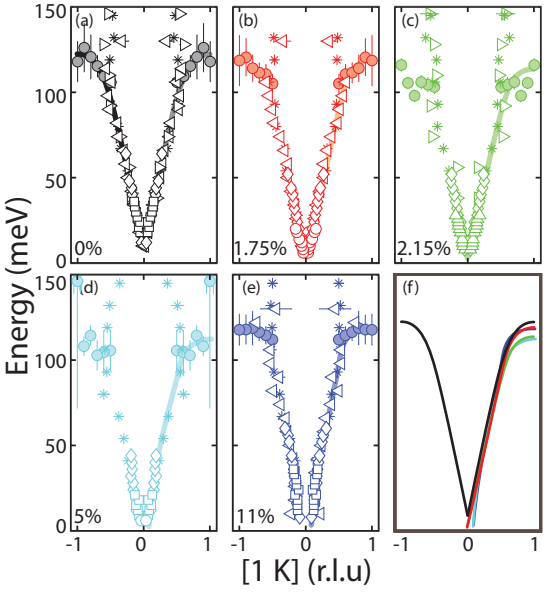

FIG. 9. (a)–(e) Dispersion along the [1 K] direction from two-Gaussian fits to constant energy cuts (open symbols) and damped harmonic-oscillator fits to constant energy cuts (filled symbols) for $x = 0$, 0.0175, 0.0215, 0.05, and 0.11, respectively. Solid lines are guides to the eye. (f) Overplot of guides from (a)–(e).

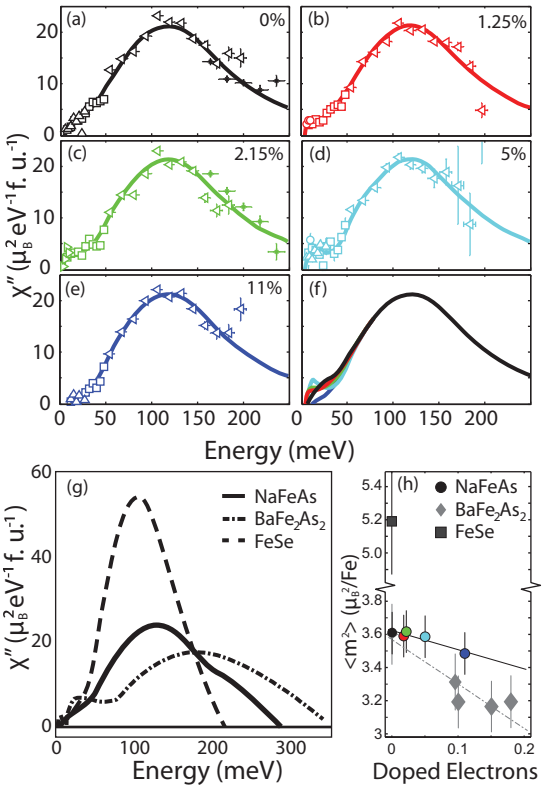

FIG. 10. Energy dependence of the local dynamic susceptibility $\chi''(E)$ in $NaFe_{1-x}Co_xAs$ in absolute units (a)–(e) for $x = 0$, 0.0175, 0.0215, 0.05, and 0.11, respectively. Solid lines are a combination of a smoothed moving average below $E = 70$ meV and a damped harmonic-oscillator fit to all data sets above 70 meV. (f) Overplot of guides from (a)–(e). (g) Energy dependence of the local susceptibility in the parent compounds of NaFeAs (solid line), $BaFe_2As_2$ (dashed-dotted line), and FeSe (dashed line). (h) Dependence of total fluctuating moment on doped electrons in $NaFe_{1-x}Co_xAs$ (circles), $BaFe_{2-x}Ni_xAs_2$ (diamonds), and FeSe (square). Solid line is a linear fit to the electron doping dependency of the moment in $NaFe_{1-x}Co_xAs$. Dashed line is an identical fitting for $BaFe_{2-x}Ni_xAs_2$

of a guide to the eye derived from a moving average of data for energy transfers below 70 meV and a damped harmonic-oscillator fit to data from all dopings above 70 meV energy transfer. The horizontal error bars indicate the energy integration range, and the vertical error bars are statistical errors from the integration. Figure 10(f) plots the solid lines from Figs. 10(a)–10(e), which reveal that $\chi''(E)$ for energies above 70 meV are virtually identical at all probed Co-doping levels. To compare these results with those obtained for the $BaFe_2As_2$ and the FeSe families of iron-based superconductors, we show in Fig. 10(g) the energy dependence of $\chi''(E)$ for FeSe (dashed line) [61], $BaFe_2As_2$ (dashed-dotted line) [64], and NaFeAs (solid line) [50]. It is clear that the spin-excitation energy bandwidth systematically decreases upon moving from $BaFe_2As_2$ to NaFeAs and then to FeSe. This is consistent with the notion that electron correlations increase from $BaFe_2As_2$ to NaFeAs, then to FeSe due to the increased iron pnictogen height from the iron plane [53,65].

To determine the total fluctuating magnetic moments of $NaFe_{1-x}Co_xAs$, defined as $\langle m^2\rangle = (3/\pi)\int \chi''(E)dE/[1 - \exp(-E/k_BT)]$ [17], and to compare the outcome with those of $BaFe_{2-x}Ni_xAs_2$ [29] and FeSe [61], we show in Fig. 10(h) the electron-doping dependence of $\langle m^2\rangle$ for the first two families of materials, where the electron doping level per iron is assumed to be the Co-doping (or 1/2 Ni-doping) level per Fe site. By overlaying the electron doping dependence of the total fluctuating magnetic moments from $BaFe_{2-x}Ni_xAs_2$ and $NaFe_{1-x}Co_xAs$, we see a systematic decrease in $\langle m^2\rangle$ with increasing electron doping. In spite of the largely different energy scales of the overall spin-excitation bandwidth for $BaFe_{2-x}Ni_xAs_2$ and $NaFe_{1-x}Co_xAs$, their total fluctuating magnetic moments are rather similar, and decrease systematically with the number of electrons added rather than irons replaced. These results reinforce the view that magnetism is important for superconductivity of iron-based superconductors regardless of how electrons are doped into these materials [6,7]. For comparison, we note that the total fluctuating moment of FeSe is about 40% larger than those of $BaFe_{2-x}Ni_xAs_2$ and $NaFe_{1-x}Co_xAs$, as shown in Fig. 10(h) [61]. This may reflect the fact that FeSe has a larger iron pnictogen height from the iron plane compared with $BaFe_{2-x}Ni_xAs_2$ and $NaFe_{1-x}Co_xAs$, suggesting that the system has stronger electron correlations and larger localized moments.

III. DISCUSSION AND CONCLUSIONS

Through a comprehensive survey of spin excitations in $NaFe_{1-x}Co_xAs$, we establish the electron-doping evolution of the spin excitation spectra for this family of iron-pnictide superconductors. Figure 11 compares the electron-doping evolution of the Fermi surfaces of $NaFe_{1-x}Co_xAs$ [66–68] and $Ba(Fe_{1-x}Co_x)_2As_2$ [62] obtained from angle-resolved photoemission spectroscopy experiments. In these schematics,

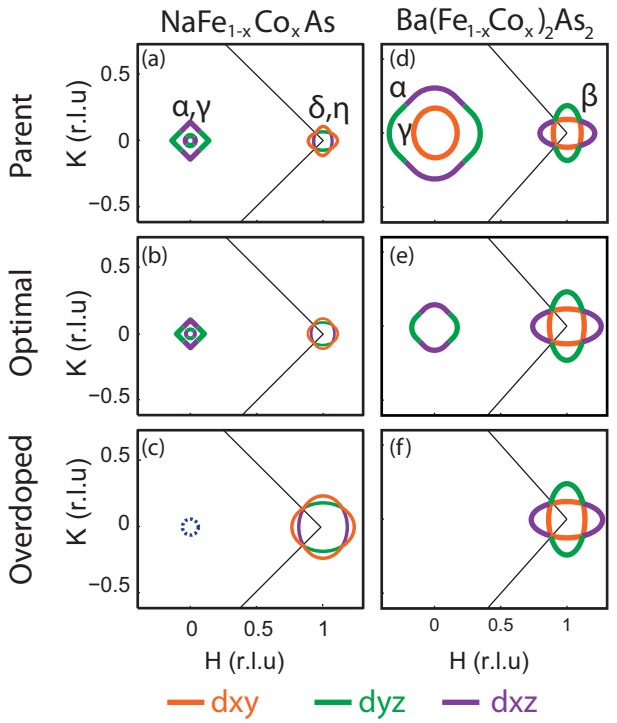

FIG. 11. Schematic Fermi surface for $NaFe_{1-x}Co_xAs$ and $Ba(Fe_{1-x}Co_x)_2As_2$ in the (a,d) parent [8,70], (b,e) optimally doped [8,71], and (c,f) overdoped [8,67] regimes, respectively. ARPES results show the α and γ bands are holelike whereas β and η are electron bands. Dashed lines indicate that a band is very near but just below the Fermi surface.

red, green, and purple lines represent Fermi surface sheets with d_{xy}, d_{yz}, and d_{xz} orbital characters of the Fe $3d$ electrons. In spite of the clear differences in the size and shape of the Fermi surfaces of undoped NaFeAs and $BaFe_2As_2$, the effects of electron-doping by partially substituting Co for Fe are similar. Namely, the electron Fermi surfaces are enlarged and the hole Fermi surfaces are drastically reduced. Superconductivity vanishes when hole pockets near Γ sink below the Fermi surface due to electron overdoping, destroying the hole-electron Fermi pocket nesting condition. This reinforces the view that while the nesting condition is not sufficient to support superconductivity, the correlation of its destruction with the disappearance of superconductivity suggests it is a necessary condition for some iron pnictides [38–40].

Our systematic measurements of the overall spin-excitation spectra in the $NaFe_{1-x}Co_xAs$ family of materials are consistent with the picture where the low-energy spin excitations are coupled with the Fermi surface nesting condition while high-energy spin excitations are much less Co-doping-dependent. The evolution of spin excitations in the $BaFe_{2-x}Ni_xAs_2$ family of materials paints a very similar picture [29]. In addition, we find that in spite of the large differences in spin-excitation bandwidth among the $NaFe_{1-x}Co_xAs$, $BaFe_{2-x}Ni_xAs_2$, and FeSe families of materials, their total spin-fluctuating moments are comparable to within ∼50% and decrease with increasing electron doping. This is surprising given that these families of iron-based superconductors have rather different crystal structures and ground states: $BaFe_2As_2$ has nearly coupled structural and magnetic phase transitions with a static ordered moment of $M = \sim 0.8\mu_B$/Fe [33], NaFeAs has separated structural and magnetic phase transitions with $M = \sim 0.1\mu_B$/Fe [49], and FeSe is a superconductor without static AF order [69]. The systematic narrowing of the spin-excitation energy bandwidths on moving from $BaFe_{2-x}Ni_xAs_2$ and $NaFe_{1-x}Co_xAs$ to FeSe may arise from the gradual narrowing of the electronic energy bandwidth due to increased iron pnictogen height and decreased electron hopping kinetic energy (and thus increased electron localization) [53,65]. In this picture, the slightly increased fluctuating moment in FeSe is due to increased electron localization in this system. The similar total spin fluctuating moments in $BaFe_{2-x}Ni_xAs_2$ and $NaFe_{1-x}Co_xAs$ suggest that the microscopic origin for magnetism, and possibly also superconductivity, is the same for these materials.

It has been widely observed that there is a gain in low-energy spin fluctuations, dubbed neutron spin resonance, upon entering the superconducting state, suggesting a close connection between superconductivity and magnetic fluctuations. Quantitatively, it is reasonable to assume a connection if the energy gain from these fluctuations across T_c is larger than the superconducting condensation energy. This was shown to be the case in $Ba_{0.67}K_{0.33}Fe_2As_2$ [28], where an exchange energy $\Delta E_{ex} = -0.66$ meV/Fe was much larger than the condensation energy $U_c = -0.09$ meV/Fe. Following the same procedure, we consider if the same is true in near optimally doped $NaFe_{0.9785}Co_{0.0215}As$. The local susceptibility above and below T_c, shown in Fig. 12(a), gives rise to an exchange energy of $\Delta E_{ex} = -0.21$ meV/Fe, while the condensation energy, calculated from the specific heat of a similarly doped compound [48], was found to be $U_c = -0.008$ meV/Fe. While these compounds have similar exchange energies, the superconductivity in $NaFe_{1-x}Co_xAs$ is substantially more fragile, and the condensation energy is several orders of magnitude smaller than the exchange energy associated with resonance. Therefore, our results are consistent with the notion that spin excitations are responsible for superconductivity in $NaFe_{1-x}Co_xAs$.

In conclusion, using ToF INS spectroscopy, we have mapped out the overall spin-excitation spectra for $NaFe_{1-x}Co_xAs$ with $x = 0$, 0.0175, 0.0215, 0.05, and 0.11. Our central conclusion is that the electron-doping evolution of the spin-excitation spectra in this family of iron pnictides is similar to those of the electron-doped $BaFe_2As_2$ family

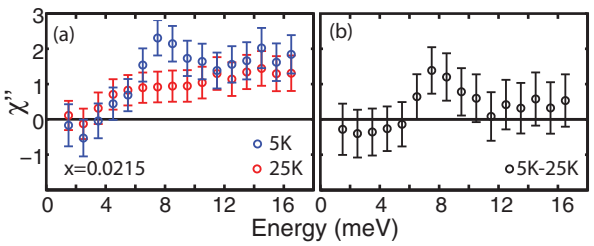

FIG. 12. (a) Background subtracted local susceptibility of $NaFe_{1-x}Co_xAs$ ($x = 0.0215$) and (b) the difference in susceptibility between the superconducting ($T = 5$ K) and normal ($T = 25$ K) state. High-temperature data are measured from the same samples and environment as other data for $x = 0.0215$ in the present report.

TABLE I. Normalization factors.

Doping	0%	1.75%	2.15%	5%	11%
Acoustic	1	0.95 ± 0.05	1.68 ± 0.19		1.75 ± 0.11
Optical	1				1.73 ± 0.11
Absolute			1.69 ± 0.19		
Given				1.9	

of materials, in spite of their large differences in structure and total magnetic excitation energy bandwidth. Given the similarities present across different families of iron pnictides, our data suggest that they share a microscopic origin for magnetism and superconductivity and highlight the coupling between their spin-excitation superconductivity [6].

ACKNOWLEDGMENTS

A special thanks to Zachary Simms, Tucker Netherton, and Caleb Redding for their significant contributions in synthesis. The single crystal synthesis and neutron scattering work at Rice University is supported by the U.S. DOE, Office of Basic Energy Sciences, under Contract No. DE-SC0012311. Part of the materials synthesis work at Rice University is supported by the Robert A. Welch Foundation Grant No. C-1839. The research at ORNL's SNS and HFIR was sponsored by the Scientific User Facilities Division, Office of Basic Energy Sciences, U.S. DOE.

APPENDIX

1. Absolute neutron-scattering intensity normalization

Typically, TOF INS data are normalized using a vanadium standard for samples with known mass in the neutron beam (see Table I). The $NaFe_{1-x}Co_2As$ system, however, is more difficult to normalize by the sample mass as there is often residual powder flux trapped in the single-crystal sample during its formation, especially at high Co-doping concentrations. This fact makes normalization purely by vanadium unreliable as the single-crystal mass contributing to coherent scattering may be lower than the weighed mass. Because we wanted to compare spin-excitation intensities directly across several dopings and with other iron-based superconductors, we sought self-consistent normalization, which could be checked against an external standard. This requires a comparison of the structural properties rather than the magnetic ones, and due to the varied incident energies measured for each composition (Table II) as well differing detector geometries, there were not many viable options. We identified one optical phonon as well as one acoustic phonon usable for self-consistent normalization and one acoustic phonon used for absolute normalization. All data shown in the Appendix from ARCS ($x = 0$, 0.0175, and 0.11) had been normalized to the same vanadium sample, and data from SEQUOIA ($x = 0.0215$) had also been normalized to standard vanadium.

TABLE II. Measured incident energy summary for $NaFe_{1-x}Co_xAs$.

Ei (meV)	0	0.0175	0.0215	0.05	0.11	Symbol
25		X		X		◯
35			X			▷
50	X				X	△
80	X	X	X	X	X	□
150	X	X			X	♢
250	X	X	X	X	X	∗
350	X		X			•
Instr	ARCS	ARCS	SEQUOIA	MAPS	ARCS	

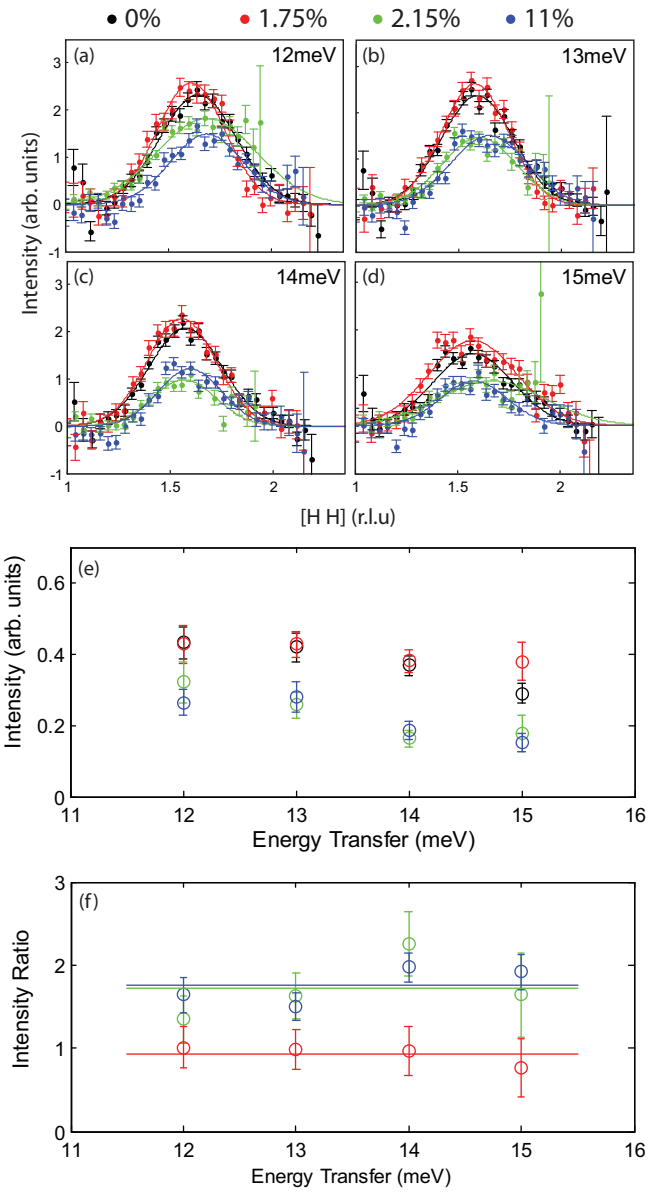

FIG. 13. Self-consistent normalization using the top of the (2,2,1) acoustic phonon. (a)–(d) Background subtracted cuts along the $[H,H]$ direction at $E = 12 \pm 0.5$, 13 ± 0.5, 14 ± 0.5, and 15 ± 0.5 meV, respectively. Dopings are noted by color and labeled at the top of the figure. Single-peak Gaussian fits are plotted in solid lines. (e) Integrated intensity for cuts in (a)–(d) is plotted as a function of energy. Integrated intensity is calculated from fits with error bars derived from fit parameters. (f) Intensity ratio ($I_{x=0}/I_x$) is plotted as a function of energy. Horizontal lines depict the weighted average of corresponding data.

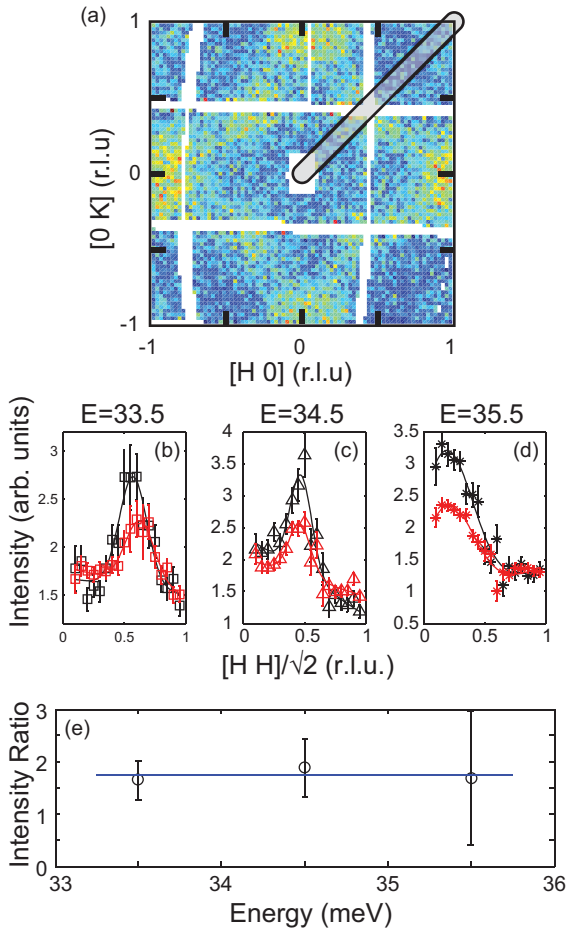

FIG. 14. (a) Optical phonon near the zone center seen with $E_i = 50$ meV and $E = 34.5 \pm 0.5$ meV. (b)–(e) Cuts through the phonon for $NaFe_{1-x}Co_xAs$ with $x = 0$ (black) and 0.11 (red). Cuts fit with single Gaussians (solid lines) constrained to share a center. (e) Ratios of integrated intensity for fits in (b)–(d). The blue line is a weighted average.

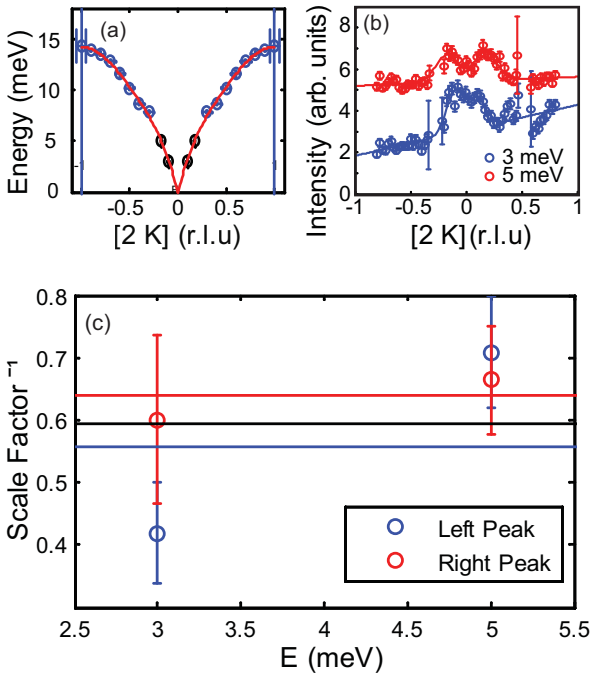

FIG. 15. (a) Acoustic phonon from (2,0,1) determined by constant E and $\mathbf{Q}$ scans. Red line is a polynomial fit used to determine the phonon speed. (b) Transverse cuts at 3 ± 1 (lower) and 5 ± 1 meV (higher) fit with two Gaussians on a linear background (solid lines). (c) Following Ref. [72], the inverse scale factor resulting from self-normalization with phonon shown in (a) and (b).

For $E_i = 250$ meV, we found it possible to see the acoustic phonon near (2,2,1) at the edge of the detector at ARCS as well as SEQUOIA. Unfortunately, the smaller detector area at MAPS prevented us from comparing the $x = 0.05$ Co-doped compound. Cuts were made at $E = 12 \pm 0.5$, 13 ± 0.5, 14 ± 0.5, and 15 ± 0.5 meV [Figs. 13(a)–13(d)] where intensity was strongest due to proper L matching. Given only modest changes to lattice parameters and the similarity in mass between cobalt and iron, changes to terms such as the dynamic structure factor are small and ignored for this discussion. Comparing integrated intensities for the phonon at different energies [Fig. 13(f)], we arrived at a set of scaling factors for self-consistent normalization (Table S1).

The second check of normalization comes from data with $E_i = 50$ meV for $x = 0$ and 0.11 doped compounds. An optical phonon is clearly seen in the energy slices from $E = 33$–36 meV moving toward (0,0) along the $[H,H]$ direction [Fig. 14(a)]. Making identical longitudinal cuts seen in Figs. 14(b)–14(d) shows that the phonon can be identified and fit with a single Gaussian curve. Using the fit parameters to calculate the intensity ratio for the overdoped compound results in an identical scaling parameter to normalization by acoustic phonons. This gave us confidence in the scaling results.

To confirm with absolute certainty that these scaling results were reliable, we used a clearly visible phonon at (2,0,1) in the $x = 0.0215$ Co-doped compound with $E_i = 35$ meV. The entire dispersion, mapped from constant $\mathbf{Q}$ and E cuts in Fig. 15(a), has different L values at the peak positions. Figure 15(b) shows constant-energy cuts along the $[2,K]$ direction for $E = 3$ and 5 meV, which show clear counterpropagating phonons. Figure 15(c) plots the scale factor obtained using different energy transfers. Energy transfers near $E = 4$ meV gave the proper value $L = 1$ and were used in the self-normalization. Using the process outlined by Xu *et al.* [72], we found a self-normalization factor nearly identical to the one derived from the self-consistent normalization to the parent compound.

2. Background subtraction

Once these scaling factors were taken into account, the high-energy part of the local susceptibility overlapped, as seen in Fig. 10(f). This brought all samples in line except for the $x = 0.05$ Co-doped compound, which, due to differing detector geometry, was not able to be included in any self-consistent normalizations. Given the universality of high-energy excitations across the phase diagram, a scale factor was chosen for the $x = 0.05$ cobalt doped sample to bring it in line. Final values for normalization scale factors can be found in Table I.

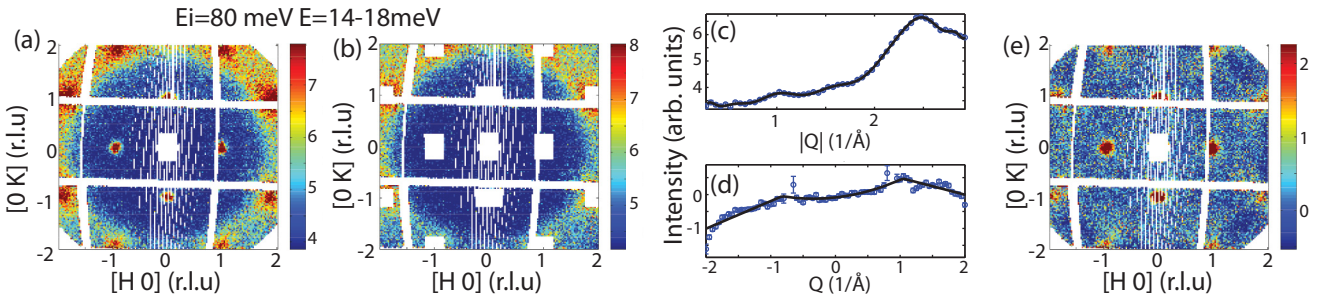

FIG. 16. Background subtraction process at low energies. Raw data (a) are masked according to the method outlined in the text (b). Ring-integrated radial data (c) and vertical linear background (d) are subtracted to give a background-free slice (e).

When desiring to directly compare intensities of TOF INS data, it is of paramount importance that care is taken when subtracting the background. Background due to the sample environment can, in principle, be determined by measuring an empty environment without a sample. We chose not to do this but instead focused our efforts on increasing counting statistics. This is reasonable considering a majority of the low-energy background is not from aluminum, but rather phonons from the sample itself. Thus, the first challenge comes from carefully fitting and subtracting the background due to low-energy phonons. Upon reaching higher energies, the spin excitations broaden as they disperse toward the zone-boundary wave vectors. Near the band top, the excitations become broad and diffusive, occupying a large fraction of the zone boundary, making it tricky to discern true intensity from the background. Distinct energy regions that we identified each require their own background fitting solution.

At low energies, the background is predominantly due to phonons and detector quirks. It should be noted that all TOF measurements were performed in the same orientation, tying the L component of $\mathbf{Q}$ to the incident and transferred energies. This is reasonable since triple-axis measurements have revealed only a weak L-dependence in spin excitations of $NaFe_{1-x}Co_xAs$ [56], removing the need to consider L values. Given that the phonons are well defined in $\mathbf{Q}$ and E, measurements made at different incident energies will result in different phonon backgrounds. Fortunately, the phonon background in the vicinity of the AF wave vector is always quite broad. This is because the AF wave vector is at the edge of the structural zone boundary, so the dispersion is already quite flat when it reaches the AF wave vector. This broad nature, alongside the high symmetry of the twinned crystal, leads to nearly isotropic features.

An example of our background fitting and subtraction process is highlighted in Fig. 16. Figure 16(a) shows the raw data with $E_i = 80$ meV at an energy transfer of $E = 16 \pm 2$ meV. We first mask the signal at AF wave vectors shown in white boxes in Fig. 16(b). We then fit a radial background by integrating rings of constant $\mathbf{Q}$ and E after masking the data [Fig. 16(c)]. Intensity was fit using a high-order polynomial with order decreasing with energy. Masking was done by fitting transverse and longitudinal cuts and omitting data within three half-width at half-maximum peak centers [Fig. 16(b)]. Additionally, we found a large background component along the vertical direction of detector tubes. In fact, each detector bank had a distinctly different profile. This may be due in part to the large asymmetry of our sample mount along the vertical direction. The background parallel to the detector tubes was also fit after subtracting the radially symmetric component [Fig. 16(d)]. A masked low-$\mathbf{Q}$ region was used for this fitting. This method was used for energy transfers below $E = 50$ meV. The background subtracted data are shown in Fig. 16(e), where we find clear magnetic excitations at the expected AF wave vectors.

For energy transfers above $E = 50$ meV, near the optical-phonon cutoff, the background becomes well behaved. It can be described well with a linear radial component and a component in the direction parallel to the detector tubes, as described above. The challenge in fitting a radial background is the increased diffusion of the signal throughout the Brillouin zone. The solution takes advantage of the lack of dispersion along the radial direction. Longitudinal and transverse cuts through the AF wave vector were fit simultaneously, restricting the background at the AF wave vector to be the same. Essentially, the background is viewed as a cone in $\mathbf{Q}$ with an offset. As such, the longitudinal cut was fit with a Gaussian atop a linear background, and the transverse cut was fit with properly constrained Gaussians atop a hyperbola. The number of Gaussians in the transverse cut were chosen empirically, with three Gaussians per side from $50 \leqslant E \leqslant 100$ meV to accommodate scattering at $[\pm 1, \pm 1]$ and two Gaussians per side from $E < 100$ meV.

[1] P. A. Lee, N. Nagaosa, and X.-G. Wen, Rev. Mod. Phys. **78**, 17 (2006).
[2] M. Eschrig, Adv. Phys. **55**, 47 (2006).
[3] J. M. Tranquada, G. Xu, and I. A. Zaliznyak, J. Magn. Magn. Mater. **350**, 148 (2014).
[4] Y. Kamihara, T. Watanabe, M. Hirano, and H. Hosono, J. Am. Chem. Soc. **130**, 3296 (2008).
[5] G. R. Stewart, Rev. Mod. Phys. **83**, 1589 (2011).
[6] D. J. Scalapino, Rev. Mod. Phys. **84**, 1383 (2012).
[7] P. C. Dai, J. Hu, and E. Dagotto, Nat. Phys. **8**, 709 (2012).
[8] P. C. Dai, Rev. Mod. Phys. **87**, 855 (2015).
[9] D. S. Inosov, C. R. Phys. **17**, 60 (2016).
[10] M. D. Lumsden, A. D. Christianson, D. Parshall, M. B. Stone, S. E. Nagler, G. J. MacDougall, H. A. Mook, K. Lokshin, T.

Egami, D. L. Abernathy, E. A. Goremychkin, R. Osborn, M. A. McGuire, A. S. Sefat, R. Jin, B. C. Sales, and D. Mandrus, Phys. Rev. Lett. **102**, 107005 (2009).
[11] S. Chi, A. Schneidewind, J. Zhao, L. W. Harriger, L. Li, Y. Luo, G. Cao, Z. Xu, M. Loewenhaupt, J. Hu, and P. C. Dai, Phys. Rev. Lett. **102**, 107006 (2009).
[12] S. Li, Y. Chen, S. Chang, J. W. Lynn, L. Li, Y. Luo, G. Cao, Z. Xu, and P. C. Dai, Phys. Rev. B **79**, 174527 (2009).
[13] D. K. Pratt, W. Tian, A. Kreyssig, J. L. Zarestky, S. Nandi, N. Ni, S. L. Bud'ko, P. C. Canfield, A. I. Goldman, and R. J. McQueeney, Phys. Rev. Lett. **103**, 087001 (2009).
[14] A. D. Christianson, M. D. Lumsden, S. E. Nagler, G. J. MacDougall, M. A. McGuire, A. S. Sefat, R. Jin, B. C. Sales, and D. Mandrus, Phys. Rev. Lett. **103**, 087002 (2009).
[15] D. S. Inosov, J. T. Park, P. Bourges, D. Sun, Y. Sidis, A. Schneidewind, K. Hradil, D. Haug, C. Lin, B. Keimer, and V. Hinkov, Nat. Phys. **6**, 178 (2010).
[16] M. Wang, H. Luo, J. Zhao, C. Zhang, M. Wang, K. Marty, S. Chi, J. W. Lynn, A. Schneidewind, S. Li, and P. C. Dai, Phys. Rev. B **81**, 174524 (2010).
[17] C. Lester, J.-H. Chu, J. G. Analytis, T. G. Perring, I. R. Fisher, and S. M. Hayden, Phys. Rev. B **81**, 064505 (2010).
[18] J. T. Park, D. S. Inosov, A. Yaresko, S. Graser, D. L. Sun, Ph. Bourges, Y. Sidis, Y. Li, J.-H. Kim, D. Haug, A. Ivanov, K. Hradil, A. Schneidewind, P. Link, E. Faulhaber, I. Glavatskyy, C. T. Lin, B. Keimer, and V. Hinkov, Phys. Rev. B **82**, 134503 (2010).
[19] H.-F. Li, C. Broholm, D. Vaknin, R. M. Fernandes, D. L. Abernathy, M. B. Stone, D. K. Pratt, W. Tian, Y. Qiu, N. Ni, S. O. Diallo, J. L. Zarestky, S. L. Bud'ko, P. C. Canfield, and R. J. McQueeney, Phys. Rev. B **82**, 140503(R) (2010).
[20] D. S. Inosov, J. T. Park, A. Charnukha, Y. Li, A. V. Boris, B. Keimer, and V. Hinkov, Phys. Rev. B **83**, 214520 (2011).
[21] M. Wang, H. Luo, M. Wang, S. Chi, J. A. Rodriguez-Rivera, D. Singh, S. Chang, J. W. Lynn, and P. C. Dai, Phys. Rev. B **83**, 094516 (2011).
[22] L. W. Harriger, H. Q. Luo, M. S. Liu, C. Frost, J. P. Hu, M. R. Norman, and P. Dai, Phys. Rev. B **84**, 054544 (2011).
[23] K. Matan, S. Ibuka, R. Morinaga, S. Chi, J. W. Lynn, A. D. Christianson, M. D. Lumsden, and T. J. Sato, Phys. Rev. B **82**, 054515 (2010); T. J. Sato, K. Matan, S. Ibuka, R. Morinaga, S. Chi, J. W. Lynn, A. D. Christianson, and M. D. Lumsden, *ibid.* **83**, 059901(E) (2011).
[24] M. Liu, L. W. Harriger, H. Luo, M. Wang, R. A. Ewings, T. Guidi, H. Park, K. Haule, G. Kotliar, S. M. Hayden, and P. C. Dai, Nat. Phys. **8**, 376 (2012).
[25] H. Q. Luo, Z. Yamani, Y. Chen, X. Lu, M. Wang, S. Li, T. A. Maier, S. Danilkin, D. T. Adroja, and P. C. Dai, Phys. Rev. B **86**, 024508 (2012).
[26] G. S. Tucker, R. M. Fernandes, H.-F. Li, V. Thampy, N. Ni, D. L. Abernathy, S. L. Bud'ko, P. C. Canfield, D. Vaknin, J. Schmalian, and R. J. McQueeney, Phys. Rev. B **86**, 024505 (2012).
[27] M. G. Kim, G. S. Tucker, D. K. Pratt, S. Ran, A. Thaler, A. D. Christianson, K. Marty, S. Calder, A. Podlesnyak, S. L. Bud'ko, P. C. Canfield, A. Kreyssig, A. I. Goldman, and R. J. McQueeney, Phys. Rev. Lett. **110**, 177002 (2013).
[28] M. Wang, C. L. Zhang, X. Lu, G. Tan, H. Luo, Y. Song, M. Wang, X. Zhang, E. A. Goremychkin, T. G. Perring, T. A. Maier, Z. Yin, K. Haule, G. Kotliar, and P. C. Dai, Nat. Commun. **4**, 2874 (2013).
[29] H. Q. Luo, X. Y. Lu, R. Zhang, M. Wang, E. A. Goremychkin, D. T. Adroja, S. Danilkin, G. Deng, Z. Yamani, and P. C. Dai, Phys. Rev. B **88**, 144516 (2013).
[30] S. Ibuka, Y. Nambu, T. Yamazaki, M. D. Lumsden, and T. J. Sato, Physica C **507**, 25 (2014).
[31] M. G. Kim, M. Wang, G. S. Tucker, P. N. Valdivia, D. L. Abernathy, S. Chi, A. D. Christianson, A. A. Aczel, T. Hong, T. W. Heitmann, S. Ran, P. C. Canfield, E. D. Bourret-Courchesne, A. Kreyssig, D. H. Lee, A. I. Goldman, R. J. McQueeney, and R. J. Birgeneau, Phys. Rev. B **92**, 214404 (2015).
[32] C. de la Cruz, Q. Huang, J. W. Lynn, J. Li, W. Ratcliff II, J. L. Zarestky, H. A. Mook, G. Chen, J. Luo, N. Wang, and P. C. Dai, Nature (London) **453**, 899 (2008).
[33] Q. Huang, Y. Qiu, W. Bao, M. A. Green, J. W. Lynn, Y. C. Gasparovic, T. Wu, G. Wu, and X. H. Chen, Phys. Rev. Lett. **101**, 257003 (2008).
[34] C. Lester, J.-H. Chu, J. G. Analytis, S. C. Capelli, A. S. Erickson, C. L. Condron, M. F. Toney, I. R. Fisher, and S. M. Hayden, Phys. Rev. B **79**, 144523 (2009).
[35] S. Nandi, M. G. Kim, A. Kreyssig, R. M. Fernandes, D. K. Pratt, A. Thaler, N. Ni, S. L. Budko, P. C. Canfield, J. Schmalian, R. J. McQueeney, and A. I. Goldman, Phys. Rev. Lett. **104**, 057006 (2010).
[36] H. Luo, R. Zhang, M. Laver, Z. Yamani, M. Wang, X. Lu, M. Wang, Y. Chen, S. Li, S. Chang, J. W. Lynn, and P. C. Dai, Phys. Rev. Lett. **108**, 247002 (2012).
[37] X. Lu, H. Gretarsson, R. Zhang, X. Liu, H. Luo, W. Tian, M. Laver, Z. Yamani, Y.-J. Kim, A. H. Nevidomskyy, Q. Si, and P. C. Dai, Phys. Rev. Lett. **110**, 257001 (2013).
[38] I. I. Mazin, Nature (London) **464**, 183 (2010).
[39] P. J. Hirschfeld, M. M. Korshunov, and I. I. Mazin, Rep. Prog. Phys. **74**, 124508 (2011).
[40] A. V. Chubukov, Annu. Rev. Condens. Matter Phys. **3**, 57 (2012).
[41] K. Haule, J. H. Shim, and G. Kotliar, Phys. Rev. Lett. **100**, 226402 (2008).
[42] Q. Si and E. Abrahams, Phys. Rev. Lett. **101**, 076401 (2008).
[43] C. Fang, H. Yao, W.-F. Tsai, J. P. Hu, and S. A. Kivelson, Phys. Rev. B **77**, 224509 (2008).
[44] C. Xu, M. Müller, and S. Sachdev, Phys. Rev. B **78**, 020501(R) (2008).
[45] C. W. Chu, F. Chen, M. Gooch, A. M. Guloy, B. Lorenz, B. Lv, K. Sasmal, Z. J. Tang, J. H. Tapp, and Y. Y. Xue, Physica (Amsterdam) C **469**, 326 (2009).
[46] D. R. Parker, M. J. P. Smith, T. Lancaster, A. J. Steele, I. Franke, P. J. Baker, F. L. Pratt, M. J. Pitcher, S. J. Blundell, and S. J. Clarke, Phys. Rev. Lett. **104**, 057007 (2010).
[47] A. F. Wang, X. G. Luo, Y. J. Yan, J. J. Ying, Z. J. Xiang, G. J. Ye, P. Cheng, Z. Y. Li, W. J. Hu, and X. H. Chen, Phys. Rev. B **85**, 224521 (2012).
[48] G. T. Tan, P. Zheng, X. C. Wang, Y. C. Chen, X. T. Zhang, J. L. Luo, T. Netherton, Y. Song, P. C. Dai, C. L. Zhang, and S. L. Li, Phys. Rev. B **87**, 144512 (2013).
[49] S. Li, C. de la Cruz, Q. Huang, G. F. Chen, T.-L. Xia, J. L. Luo, N. L. Wang, and P. C. Dai, Phys. Rev. B **80**, 020504(R) (2009).
[50] C. L. Zhang, L. W. Harriger, Z. P. Yin, W. C. Lv, M. Y. Wang, G. T. Tan, Y. Song, D. L. Abernathy, W. Tian, T. Egami,

K. Haule, G. Kotliar, and P. C. Dai, Phys. Rev. Lett. **112**, 217202 (2014).
[51] G. Kotliar, S. Y. Savrasov, K. Haule, V. S. Oudovenko, O. Parcollet, and C. A. Marianetti, Rev. Mod. Phys. **78**, 865 (2006).
[52] K. Haule, C.-H. Yee, and K. Kim, Phys. Rev. B **81**, 195107 (2010).
[53] Z. P. Yin, K. Haule, and G. Kotliar, Nat. Phys. **10**, 845 (2014).
[54] J. Spalek, Acta Phys. Pol. A **111**, 409 (2007).
[55] C. L. Zhang, H.-F. Li, Y. Song, Y. Su, G. T. Tan, T. Netherton, C. Redding, S. V. Carr, O. Sobolev, A. Schneidewind, E. Faulhaber, L. W. Harriger, S. L. Li, X. Y. Lu, D.-X. Yao, T. Das, A. V. Balatsky, Th. Brückel, J. W. Lynn, and P. C. Dai, Phys. Rev. B **88**, 064504 (2013).
[56] C. L. Zhang, R. Yu, Y. Su, Y. Song, M. Y. Wang, G. T. Tan, T. Egami, J. A. Fernandez-Baca, E. Faulhaber, Q. Si, and P. C. Dai, Phys. Rev. Lett. **111**, 207002 (2013).
[57] C. L. Zhang, Y. Song, L.-P. Regnault, Y. Su, M. Enderle, J. Kulda, G. T. Tan, Z. C. Sims, T. Egami, Q. Si, and P. C. Dai, Phys. Rev. B **90**, 140502(R) (2014).
[58] D. L. Abernathy, M. B. Stone, M. J. Loguillo, M. S. Lucas, O. Delaire, X. L. Tang, T. Y. Lin, and B. Fultz, Rev. Sci. Instrum. **83**, 015114 (2012).
[59] G. E. Granroth, D. H. Vandergriff, and S. E. Nagler, Physica B **385-386**, 1104 (2006).
[60] N. Spyrison, M. A. Tanatar, K. Cho, Y. Song, P. C. Dai, C. L. Zhang, and R. Prozorov, Phys. Rev. B **86**, 144528 (2012).
[61] Q. Wang, Y. Shen, B. Pan, X. Zhang, K. Ikeuchi, K. Iida, A. D. Christianson, H. C. Walker, D. T. Adroja, M. Abdel-Hafiez, X. Chen, D. A. Chareev, A. N. Vasiliev, and J. Zhao, arXiv:1511.02485.
[62] P. Richard, T. Sato, K. Nakayama, T. Takahashi, and H. Ding, Rep. Prog. Phys. **74**, 124512 (2011).
[63] J. H. Zhang, R. Sknepnek, and J. Schmalian, Phys. Rev. B **82**, 134527 (2010).
[64] L. W. Harriger, M. S. Liu, H. Q. Luo, R. A. Ewings, C. D. Frost, T. G. Perring, and P. C. Dai, Phys. Rev. B **86**, 140403(R) (2012).
[65] Z. P. Yin, K. Haule, and G. Kotliar, Nat. Mater. **10**, 932 (2011).
[66] Z.-H. Liu, P. Richard, K. Nakayama, G.-F. Chen, S. Dong, J.-B. He, D.-M. Wang, T.-L. Xia, K. Umezawa, T. Kawahara, S. Souma, T. Sato, T. Takahashi, T. Qian, Y. Huang, N. Xu, Y. Shi, H. Ding, and S.-C. Wang, Phys. Rev. B **84**, 064519 (2011).
[67] S. T. Cui, S. Y. Zhu, A. F. Wang, S. Kong, S. L. Ju, X. G. Luo, X. H. Chen, G. B. Zhang, and Z. Sun, Phys. Rev. B **86**, 155143 (2012).
[68] Q. Q. Ge, Z. R. Ye, M. Xu, Y. Zhang, J. Jiang, B. P. Xie, Y. Song, C. L. Zhang, P. C. Dai, and D. L. Feng, Phys. Rev. X **3**, 011020 (2013).
[69] F.-C. Hsu, J.-Y. Luo, K.-W. Yeh, T.-K. Chen, T.-W. Huang, P. M. Wu, Y.-C. Lee, Y.-L. Huang, Y.-Y. Chu, D.-C. Yan, and M.-K. Wu, Proc. Natl. Acad. Sci. (U.S.A.) **105**, 14262 (2008).
[70] C. He, Y. Zhang, X. F. Wang, J. Jiang, F. Chen, L. X. Yang, Z. R. Ye, F. Wu, M. Arita, K. Shimada, H. Namatame, M. Taniguchi, X. H. Chen, B. P. Xie, and D. L. Feng, J. Phys. Chem. Solids **72**, 479 (2010).
[71] Z. R. Ye, Y. Zhang, F. Chen, M. Xu, J. Jiang, X. H. Niu, C. H. P. Wen, L. Y. Xing, X. C. Wang, C. Q. Jin, B. P. Xie, and D. L. Feng, Phys. Rev. X **4**, 031041 (2014).
[72] G. Xu, Z. Xu, and J. M. Tranquada, Rev. Sci. Instrum. **84**, 083906 (2013).